UC Berkeley
UC Berkeley Previously Published Works

Title

Electrochemically scrambled nanocrystals are catalytically active for CO2-to-multicarbons

Permalink

Journal

ISSN

Authors

Li, Yifan
Kim, Dohyung
Louisia, Sheena
et al.

Publication Date

DOI

Peer reviewed

Electrochemically scrambled nanocrystals are catalytically active for CO$_2$-to-multicarbons

Yifan Li[a,b,1], Dohyung Kim[a,b,c,1], Sheena Louisia[a,b], Chenlu Xie[a], Qiao Kong[a], Sunmoon Yu[b,c], Tom Lin[c], Shaul Aloni[d], Sirine C. Fakra[e], and Peidong Yang[a,b,c,f,2]

[a]Department of Chemistry, University of California, Berkeley, CA 94720; [b]Chemical Sciences Division, Lawrence Berkeley National Laboratory, Berkeley, CA 94720; [c]Department of Materials Science and Engineering, University of California, Berkeley, CA 94720; [d]The Molecular Foundry, Lawrence Berkeley National Laboratory, Berkeley, CA 94720; [e]Advanced Light Source, Lawrence Berkeley National Laboratory, Berkeley, CA 94720; and [f]Kavli Energy Nanosciences Institute, Berkeley, CA 94720

Promotion of C–C bonds is one of the key fundamental questions in the field of CO$_2$ electroreduction. Much progress has occurred in developing bulk-derived Cu-based electrodes for CO$_2$-to-multicarbons (CO$_2$-to-C$_{2+}$), especially in the widely studied class of high-surface-area "oxide-derived" copper. However, fundamental understanding into the structural characteristics responsible for efficient C–C formation is restricted by the intrinsic activity of these catalysts often being comparable to polycrystalline copper foil. By closely probing a Cu nanoparticle (NP) ensemble catalyst active for CO$_2$-to-C$_{2+}$, we show that bias-induced rapid fusion or "electrochemical scrambling" of Cu NPs creates disordered structures intrinsically active for low overpotential C$_{2+}$ formation, exhibiting around sevenfold enhancement in C$_{2+}$ turnover over crystalline Cu. Integrating ex situ, passivated ex situ, and in situ analyses reveals that the scrambled state exhibits several structural signatures: a distinct transition to single-crystal Cu$_2$O cubes upon air exposure, low crystallinity upon passivation, and high mobility under bias. These findings suggest that disordered copper structures facilitate C–C bond formation from CO$_2$ and that electrochemical nanocrystal scrambling is an avenue toward creating such catalysts.

electrocatalysis | nanomaterials | CO$_2$ reduction | structure dynamics

Structural evolution of materials under operation is a topic of emergent importance in the field of heterogeneous catalysis (1). Since nanoscale catalysts are highly susceptible to structural changes due to their high surface area and energetics, growing awareness of this phenomenon has led to deeper understanding of catalysis from a spectrum of works in both gas and liquid phase (1–4). The catalytic relevance of such dynamics to CO$_2$ electrocatalysis has recently been highlighted in copper-based systems (5–8).

Understanding the structural requirements of copper to promote CO$_2$ electroconversion to multicarbon products (CO$_2$-to-C$_{2+}$) is crucial for the development of catalyst materials in the field. With copper as the sole material to demonstrate CO$_2$-to-C$_{2+}$ at reasonable rate and efficiency (9), a host of high-activity copper catalysts have shown promise in achieving high C$_{2+}$ activity/selectivity in bulk product formation rates (10–17). However, the intrinsic CO$_2$-to-C$_{2+}$ activity (e.g., μA$_{C2+}$/cm$^2_{Cu}$) of many of these catalysts only marginally improves against a typical copper foil surface thus far, suggesting that nominal activity enhancements are inextricable from the modulation of extrinsic factors, such as local pH or mass transport, through catalyst microstructure (9). Hence, despite many investigations into the structural and/or compositional origin of CO$_2$-to-C$_{2+}$ (14, 15, 18–21), only few reports identify a core structural variable that correlates with and directly influences the intrinsic CO$_2$-to-C$_{2+}$ activity (22). We ascribe this discrepancy largely to two difficulties: 1) enriching the active surface on bulk-processed copper catalysts and 2) the tendency for materials to transform under electrochemical conditions.

Recently, we reported the structural transformation of a copper nanoparticle (Cu NP) ensemble into cuboidal structures, coupled with selective electroconversion of CO$_2$ to multicarbons at lowered overpotentials (23). The observed coalescence of NPs toward distinct shape formation and desirable catalytic performance, in contrast to conventional sintering and deactivation, warrants a close study of the electrochemical evolution process. In light of both the prevalence of structural dynamics on copper nanocatalysts and the importance of understanding structural effects on intrinsic activity, such work may enable directed evolution strategies as new avenues to electrocatalyst development for CO$_2$ utilization.

In this work, we probe the structural transformation process of the previously reported Cu NP ensembles under CO$_2$ electro-reducing conditions. By closely tracking the material state over electrolysis, an ex situ structural signature (i.e., single crystalline oxide nanocubes) is identified and confirmed to be unique to the C$_{2+}$ active catalyst. This signature is determined to result from oxidation after removal of bias; hence, a chemical passivation technique is employed to impede this oxidation. Subsequent passivated ex situ characterization reveals a second signature: low crystallinity or enriched disorder, boosting the intrinsic C$_{2+}$ activity by sevenfold over crystalline counterparts. Further in situ

Significance

The electrocatalytic conversion of CO$_2$ to value-added products, especially valuable multicarbon products, is a pathway toward sustainable formation of chemicals and fuels typically derived from fossil fuels, while mitigating CO$_2$ emissions. Fundamental understanding and development of more efficient catalysts for this reaction require deep investigation into structures with high intrinsic activity, which are limited at present. This work comprehensively investigates a dynamic copper nanoparticle ensemble catalyst that significantly improves intrinsic activity of copper for multicarbon formation. Through concerted ex situ and in situ characterization techniques, it illustrates an electrochemically induced fusion of copper nanoparticles that result in a catalytically active disordered structure, motivating closer study of disordered metal nanostructures for C–C coupling electrocatalysis.

characterization suggests that the disordered state arises in part due to a high mobility of the initial state, resulting in a rapid transformation on a time scale of seconds. Together, these three lines of characterization illustrate a phenomenon we term "electrochemical scrambling," in which cathodic bias induces the rapid fusion of nanocrystals into an active disordered state, highly susceptible to concurrent oxidation and crystallization upon exposure to ambient conditions. These findings motivate the closer study of disordered surfaces as structural characteristics responsible for enhancing CO_2-to-C_{2+} turnover and raise the prospect of structural dynamics as an approach to catalyst design.

Results and Discussion

Colloidally synthesized Cu NPs (7 nm) were spread on carbon paper and biased in CO_2 electroreducing conditions for multicarbon production in an aqueous H-cell environment (0.1 M $KHCO_3$). The observed change by ex situ characterization is rapid and striking, with the appearance of cubic structures on the order of seconds and the predominance of these structures on the order of minutes (Fig. 1A and *SI Appendix*, Fig. S1). More negative potentials resulted in a more rapid evolution process (*SI Appendix*, Fig. S2). Regardless, the evolution of NPs under these biases eventually resulted in identical catalysts by both their morphology and catalytic activity (*SI Appendix*, Fig. S3).

Qualitatively, the evolution is described by the loss of original NPs, being gradually replaced by cubic and cuboidal structures (Fig. 1B). The formation of cubes (Fig. 1C) is surprising given that the original NPs are spherical and exhibit fivefold twinned Cu (*SI Appendix*, Fig. S4). Furthermore, high-resolution transmission electron microscopy (HRTEM) reveals that these cubes are single-crystalline Cu_2O (Fig. 1D). These observations are beyond the irregularly shaped structures typically expected from NP coalescence (24, 25). The copper appears to redistribute over the course of evolution, such that at intermediary time points when many particles have transformed the resultant cubes are smaller and more uniformly spread. Indeed, the 10- to 20-nm particles at later times are characterized as monocrystalline Cu_2O cuboids as well (*SI Appendix*, Fig. S5). The prevalence of these structures with high crystallinity is confirmed on the ensemble by X-ray diffraction, most clearly seen at early time points (*SI Appendix*, Fig. S6). The Cu_2O cubes grow with no preferred orientation on the graphitic support (*SI Appendix*, Fig. S7), suggesting the absence of interaction with the support as part of the process.

To quantitatively assess the evolution of metal/oxide phase distribution, ex situ Cu K-edge X-ray absorption near-edge structure (XANES) experimental spectra were least-square linear combination-fitted (LCF) using component phases. The XANES of the original Cu NPs was used alongside Cu^0 and Cu_2O standards for a three-component LCF at early time points (Fig. 2A). The Cu NPs are suitable as a phase component as they are observed at those times by microscopy, and their XANES exhibits unique features poorly accounted for by other standard Cu phases (*SI Appendix*, Fig. S8). The relative phase portions were extracted from the XANES spectra as the evolution proceeds (*SI Appendix*, Fig. S9).

Cursory analysis of the time series (Fig. 2B) shows a rapid increase in intensity of the rising edge $1s \rightarrow 4p_{x,y}$ shake-down feature (~8,984 eV) and a fingerprint crest (~9,015 eV) indicative of Cu_2O (26). Quantitative tracking by LCF more visibly demonstrates that the early loss of Cu NPs is counterbalanced by a rapid growth of Cu_2O cubes (Fig. 2C). Beyond this critical period of Cu_2O formation ending around 600 s, most of the steady-state structure is characterized by the retention of cuboidal Cu_2O crystals. At more negative potentials, the phase evolution is accelerated but results in a similar final phase distribution (*SI Appendix*, Fig. S10). The minor metallic Cu phase is mainly found at the junctions of aggregates of Cu_2O cubes and less frequently in polycrystalline particles with no distinct morphology (*SI Appendix*, Fig. S11). Thus, ex situ XANES further confirms that the evolution of Cu NPs results in Cu_2O cuboidal rich structures as first identified using ex situ electron microscopy.

To evaluate the catalytic relevance of the appearance of Cu_2O cuboids, we considered two methods of varying the original evolved Cu NP system (sample O). First, larger 14-nm Cu NPs (sample L) were synthesized to controllably change the starting state of the material (*SI Appendix*, Fig. S12). The characteristic cube formation is absent for these larger particles under similar electrochemical conditions (*SI Appendix*, Fig. S13). Furthermore, the phase distribution remains mostly metallic throughout electrolysis (*SI Appendix*, Fig. S14). Second, we also aimed to disrupt the evolution process of the original NPs by applying a voltammetric
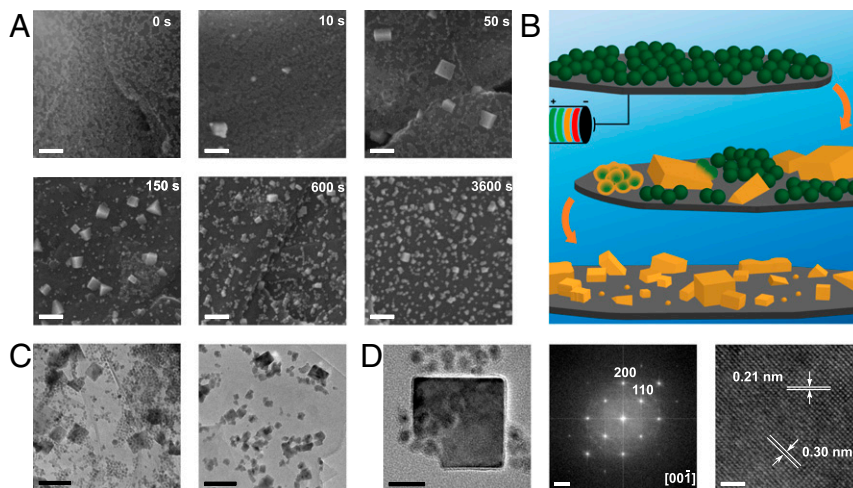
Fig. 1. Ex situ electron microscopy of the Cu NP ensemble evolution timeline. (A) SEM after removing the electrode at various time points of bias. (Scale bars, 100 nm.) (B) Schematic of the structural evolution. (C) TEM after 50 s (*Left*) and 3,600 s (*Right*) of bias. (Scale bars, 50 nm.) (D) HRTEM (Scale bar, 10 nm) of a single Cu_2O cube at 50 s with fast Fourier transform showing Cu_2O reflections (Scale bar, 2 nm^{-1}) and a selected region at higher magnification (Scale bar, 2 nm). Electrochemical conditions are −0.6 V vs. RHE in 0.1 M $KHCO_3$ at 1 atm CO_2.
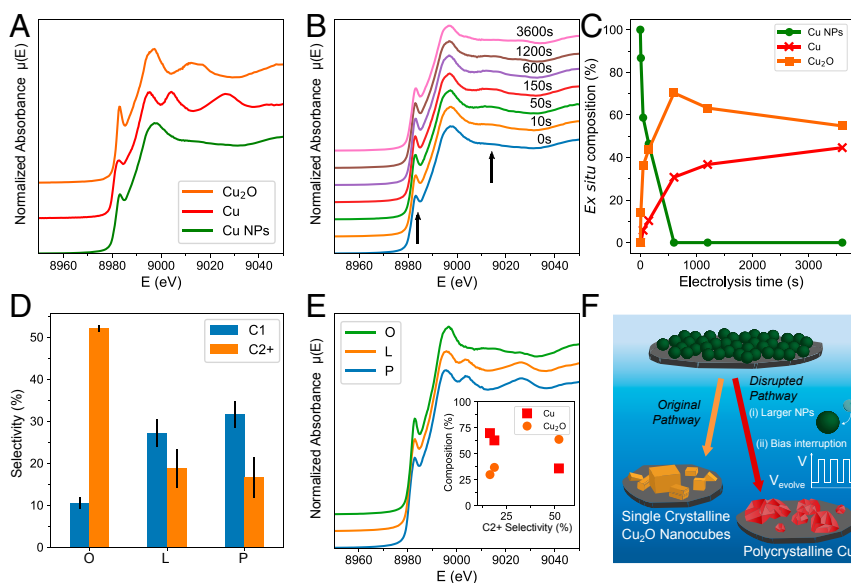
Fig. 2. Ex situ Cu K-edge XANES spectroscopy of catalysts. (*A*) Three standards used in this work: Cu, Cu_2O, and 7-nm Cu NPs. (*B*) XANES time series over electrolysis (−0.6 V vs. RHE) time ex situ with arrows indicating Cu_2O features. (*C*) Shift in composition tracked by LCF. (*D*) Catalytic selectivity for C_1 and C_{2+} products in samples O, L, and P (error bars 1 SD, *n* = 3) at −0.8 V vs. RHE. (*E*) XANES of O, L, and P after 1 h at −0.8 V vs. RHE. (*Inset*) The correlation of phase composition and C_{2+} selectivity. (*F*) Scheme summarizing the catalytic relevance of the Cu_2O structures observed uniquely in sample O.

pulse perturbation program. The perturbation is applied at frequent intervals throughout the critical period of evolution, interrupting the transformation with a mild oxidation pulse (*SI Appendix*, Fig. S15). As a result, despite beginning with the same NPs, the pulsed electrode (sample P) consists of larger, more irregular morphologies compared to sample O (*SI Appendix*, Fig. S16).

A substantial reduction of C_{2+} formation is observed for samples L and P relative to O (Fig. 2*D* and *SI Appendix*, Fig. S17), in conjunction with a more metallic composition by XANES (Fig. 2*E* and *SI Appendix*, Figs. S14 and S18) and more polycrystalline aggregates of Cu as opposed to cuboidal oxides (*SI Appendix*, Fig. S19). As such, we find that the catalytic variants lacking C_{2+} selectivity also have lower Cu_2O signature in their ex situ composition (Fig. 2 *E*, *Inset* and *SI Appendix*, Table S1). These ex situ single-crystalline cuboidal Cu_2O structures are therefore a signature for catalytically enhanced C_{2+} formation. Variations of the evolution pathway, either by modifying the initial state or by perturbing the evolution process, shift the distribution of catalyst structures toward polycrystalline NPs with a high proportion of metallic Cu postreaction, correlated with lower activity for C_{2+} formation (Fig. 2*F*).

However, formation of Cu_2O is thermodynamically disfavored under CO_2 reducing conditions (27, 28), suggesting that the Cu_2O cubes should not have formed in situ. Indeed, when Cu_2O nanocubes are directly grown on the carbon support, activity is strictly limited to hydrogen evolution and C_1 formation at potentials where sample O makes majority multicarbons (*SI Appendix*, Fig. S20). Furthermore, Cu_2O electrochemically grown on carbon, after CO_2 electrolysis, is dominated by metallic Cu consisting of small particles and broken cubes with their facets destroyed (*SI Appendix*, Fig. S21). Hence, neither crystalline cubic Cu_2O itself nor its reduced equivalent is the active phase in the transformed Cu NP ensemble, despite the above ex situ observations. These findings suggest that a different structure, most likely metallic, is formed in situ and is uniquely active for CO_2-to-C_{2+}. Moreover, the structure readily and distinctively oxidizes to the single-crystal Cu_2O cubic signature at open circuit. To identify this structure, we employed a chemical immersion

passivation method using benzotriazole (BTA), which is known to prevent copper oxidation (Fig. 3*A*) (29). Immersion into a BTA solution immediately postelectrolysis coordinates BTA to the surface, preventing the formation of Cu_2O single crystals and preserving more of the underlying metallic portion as characterized by XANES, X-ray diffraction, scanning transmission electron microscopy coupled with electron energy loss spectroscopy (STEM-EELS), and X-ray photoelectron spectroscopy (XPS) (*SI Appendix*, Figs. S22–S25).

Cu K-edge extended X-ray absorption fine structure (EXAFS) was then used to probe the difference between the three catalysts when oxidation is inhibited by BTA (O-BTA, L-BTA, and P-BTA). A clear feature of O-BTA is the lower scattering amplitude from the first Cu shell of the metallic phase at 2.1 Å, with its subsequent shells following a similar trend (Fig. 3*B*). These EXAFS spectra were then fit in *q*-space to derive a numerical description of the coordination environment (*SI Appendix*, Fig. S26). The EXAFS-derived fitting parameter N_{Cu-Cu1} is used here as a quantitative descriptor of this empirical scattering amplitude difference. According to the fits (*SI Appendix*, Table S2), O-BTA exhibits a considerably lower N_{Cu-Cu1} (3.0) compared to the other catalysts L-BTA (N_{Cu-Cu1} = 6.8) and P-BTA (N_{Cu-Cu1} = 6.5). To contextualize this trend, a series of NPs with varying size and well-defined crystallinity were employed as standards (*SI Appendix*, Fig. S27). The EXAFS-derived N_{Cu-Cu1} is expected to decrease for smaller-sized NPs (*SI Appendix*, Figs. S28 and S29) by the rise in the surface area-to-volume ratio (SA/Vol); however, N_{Cu-Cu1} for O-BTA is unexpectedly low given its size of structures (~20 nm). Furthermore, all three BTA-passivated samples are composed of similarly sized nanostructures (*SI Appendix*, Fig. S30) and therefore the difference in SA/Vol does not sufficiently explain the difference in N_{Cu-Cu1} between O-BTA and L/P-BTA.

Low N_{Cu-Cu1} can result not only from having a higher portion of atoms with missing neighbors but also by local atomic disorder, which leads to destructive interference of the scattered X-rays (30). A chemical effect should also be considered—the imperfectly passivating effect of BTA results in some remnant oxide as evidenced by the rise in amplitude at 1.5 Å, which would
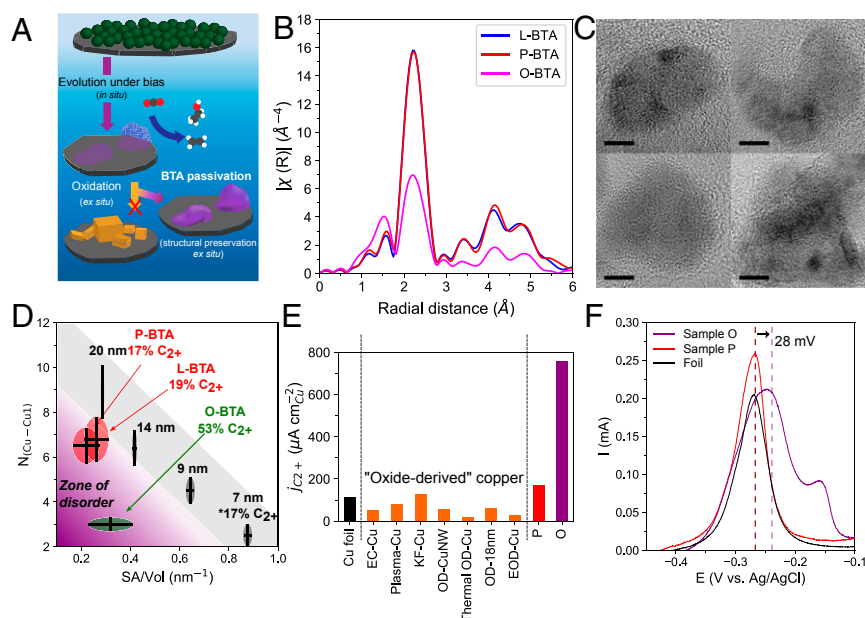
Fig. 3. Ex situ elucidation of the disordered C–C active surface. (*A*) BTA passivation diverts oxidation of the active catalyst for characterization. (*B*) R-space EXAFS of BTA-passivated O, L, and P after 1 h at −0.8 V vs. RHE. (*C*) HRTEMs of O-BTA. (Scale bar, 5 nm.) (*D*) Relationship between SA/Vol and N_{Cu-Cu1}, showing unusually low coordination of O-BTA. Error bars are 1 SD (see *SI Appendix, Supplementary Discussion S1* for details on SA/Vol and *SI Appendix*, Figs. S26 and S28 for EXAFS fit details). Isolated 7-nm NPs catalytic activity from previous work at −0.8 V vs. RHE (23). (*E*) Specific ECSA-normalized C_{2+} partial current density at −0.8 V vs. RHE for foil (14), high-performance oxide-derived catalysts from literature (see *SI Appendix*, Fig. S36 for details), P, and O. (*F*) Desorption of underpotentially deposited Pb as an indicator for adsorbate binding strength, where sample O exhibits anodic shifts (peaks at −0.25 and −0.16 V vs. Ag/AgCl) associated with its disordered surface. Dashed lines represent centroids for each anodic stripping voltammogram.

partially contribute to a lower observed N_{Cu-Cu1}. Nevertheless, crystalline domains in O-BTA are difficult to detect by HRTEM (Fig. 3*C*), in contrast with L/P-BTA where extended metallic domains are easily identified (*SI Appendix*, Fig. S31). Nanobeam electron diffraction (NBED) (*SI Appendix*, Fig. S32) suggests a relative lack of crystallinity in O-BTA as well. Meanwhile, control experiments on model Cu-based nanocrystal systems (i.e., single nanocrystals and the original fivefold twinned NPs) confirm that BTA coordination alone is insufficient to disrupt the inherent crystallinity of a Cu nanostructure (*SI Appendix*, Figs. S33 and S34). Therefore, despite some limitations of the BTA immersion technique, the overall implication of a disordered active structure is considered the most likely interpretation of these results.

These observations indicate that O-BTA achieves a unique state of structural disorder characterized by a low EXAFS-derived N_{Cu-Cu1} at low SA/Vol (Fig. 3*D*; calculation details in *SI Appendix, Supplementary Discussion S1*). L/P-BTA exhibit similarly low SA/Vol but higher N_{Cu-Cu1}, indicating that higher crystalline order is linked to their lower C_{2+} selectivity. Furthermore, low N_{Cu-Cu1} achieved by high SA/Vol in a crystalline state is likewise insufficient to attain high C_{2+} selectivity at low overpotentials, as evidenced by the activity of isolated small Cu NPs (Fig. 3*D*) (23). These findings strongly suggest that the electrochemical "scrambling" of the original NPs creates a disordered active surface (low N_{Cu-Cu1} with low SA/Vol) catalytically favorable for CO_2-to-multicarbons. Previous works have conjectured C_{2+}-boosting effects of tuning binding strength of key intermediates, especially *CO, on diverse and under-coordinated copper surfaces (15, 21, 31). Accordingly, a host of high-activity oxide-derived copper catalysts may present such disordered surface sites. However, the direct identification/quantitation of disorder in these catalysts and its effect on binding has not emerged, likely because the large volume involved of the necessary copper oxides as precursors (e.g.,

oxidized Cu foils) yields a large proportion of bulk atoms that are catalytically irrelevant but spectroscopically obtrusive for ensemble characterization. Furthermore, because such OD-Cu catalysts tend to have high roughness factors, they may present a complex mix of disordered/undercoordinated active sites and catalytically inactive copper surfaces, one possible explanation for the lack of intrinsic activity increase previously observed (9).

To quantify the enhancement of intrinsic C–C activity owing to the disordered Cu resulting from electrochemical NP scrambling, we estimated the electrochemical surface area (ECSA)-normalized specific C_{2+} activity ($\mu A/cm^2_{Cu}$) of the catalysts using lead underpotential deposition to measure Cu ECSA (*SI Appendix*, Fig. S35 and *Supplementary Discussion S2*). Sample O exhibits a considerable sevenfold increase in C_{2+} activity to that of a Cu foil, whereas the polycrystalline sample P exhibits only a minor increase (Fig. 3*E*). OD-Cu catalysts (10, 14–16) that show high performance by typically presented metrics such as F.E. (*SI Appendix*, Fig. S36) demonstrate similar or lower intrinsic activity to sample P or Cu foil as well (9). In contrast, the enrichment of disorder on sample O is directly responsible for a higher C–C dimerization activity per copper surface available, ranging from 6- to 40-fold enhancement over a representative spread of OD-Cu catalysts (Fig. 3*E* and *SI Appendix*, Fig. S37) at moderate overpotentials [−0.8 V vs. the reversible hydrogen electrode (RHE)].

The high degree of disorder exhibited by sample O is expected to result in a large concentration of strong binding sites for the key intermediate *CO, thereby increasing the probability and rate of C–C dimerization. Desorption of underpotentially deposited Pb adatoms sheds some light into the Cu surface (Fig. 3*F*). Sample P and Cu foil both exhibit anodic stripping of Pb in the same potential region of around −0.27 V vs. Ag/AgCl. Meanwhile, sample O exhibits Pb desorption peaks (−0.25 and −0.16 V vs. Ag/AgCl) that are quite anodically shifted compared to sample P or Cu foil (−0.27 V vs. Ag/AgCl),

resulting in a +28-mV shift in the centroid of the anodic stripping wave. In particular, the salient component at −0.16 V is not observed in the crystalline Cu samples in this work or in previous studies of Pb underpotential stripping on polycrystalline Cu surfaces composed of common low-index facets or on single-crystal Cu (32, 33). This indicates that sample O contains a prevalence of Cu surfaces that should have stronger electrochemical binding to adsorbates, with a lower presence of the sites on the crystalline counterpart (i.e., Cu foil) that exhibit weaker binding. The anodic shift is drastically diminished when the catalyst oxidizes to the characteristic single-crystal Cu_2O cubes, where the reduced equivalent is not disordered as before (*SI Appendix*, Fig. S38). It is also observed in a greatly reduced manner on a representative OD-Cu catalyst (*SI Appendix*, Fig. S38), which explains the low intrinsic C_{2+} activity resulting from their large portion of inactive Cu surfaces. Hence, enhanced C–C activity in sample O stems from the concentration of structural disorder, which creates surfaces of increased electrochemical binding strength to catalytic intermediates.

To determine whether any signature of the evolution can be observed in situ, we used liquid cell electrochemical (EC) XANES and (S)TEM to directly visualize their formation from the starting NP ensemble (Fig. 4A). Upon reductive bias, the EC-XANES shows a rapid (<40 s) transition to metallic Cu (Fig. 4B),

which develops its characteristic oxidized feature after exposure to ambient conditions (*SI Appendix*, Fig. S39). This confirms that the phase of the in situ active structure is Cu^0, formed almost immediately upon bias, and that Cu_2O only develops afterward at open circuit.

NP evolution was also visually tracked by EC–high-angle annular dark-field (HAADF)–STEM (*SI Appendix*, Fig. S40). An electrochemical potential of −0.6 V vs. the internal reference electrode (C/Pt) was selected to induce electrochemical evolution and cathodic current, but without rupturing the cell from vigorous gas product formation. Based on water-splitting cyclic voltammetry control experiments within the cell, this potential is negative of the onset potential for the hydrogen evolution reaction (*SI Appendix*, Fig. S41). Within a second of bias, ~20-nm structures appear to grow from the 7-nm NPs (Fig. 4C, Movie S1, and *SI Appendix*, Fig. S42). When the EC-TEM cell is then dried at ambient conditions, cubic structures are commonly found on the electrodes, which are characterized as single-crystal Cu_2O (Fig. 4D and *SI Appendix*, Fig. S43), confirming that catalytically relevant structures have formed for the biasing period of EC-TEM. In contrast, larger (15- to 20-nm) NPs do not undergo much structural change even after 60 s of bias (Movie S2 and *SI Appendix*, Fig. S44), as expected from the postelectrolysis structures of sample L that indicate minimal movement (*SI*
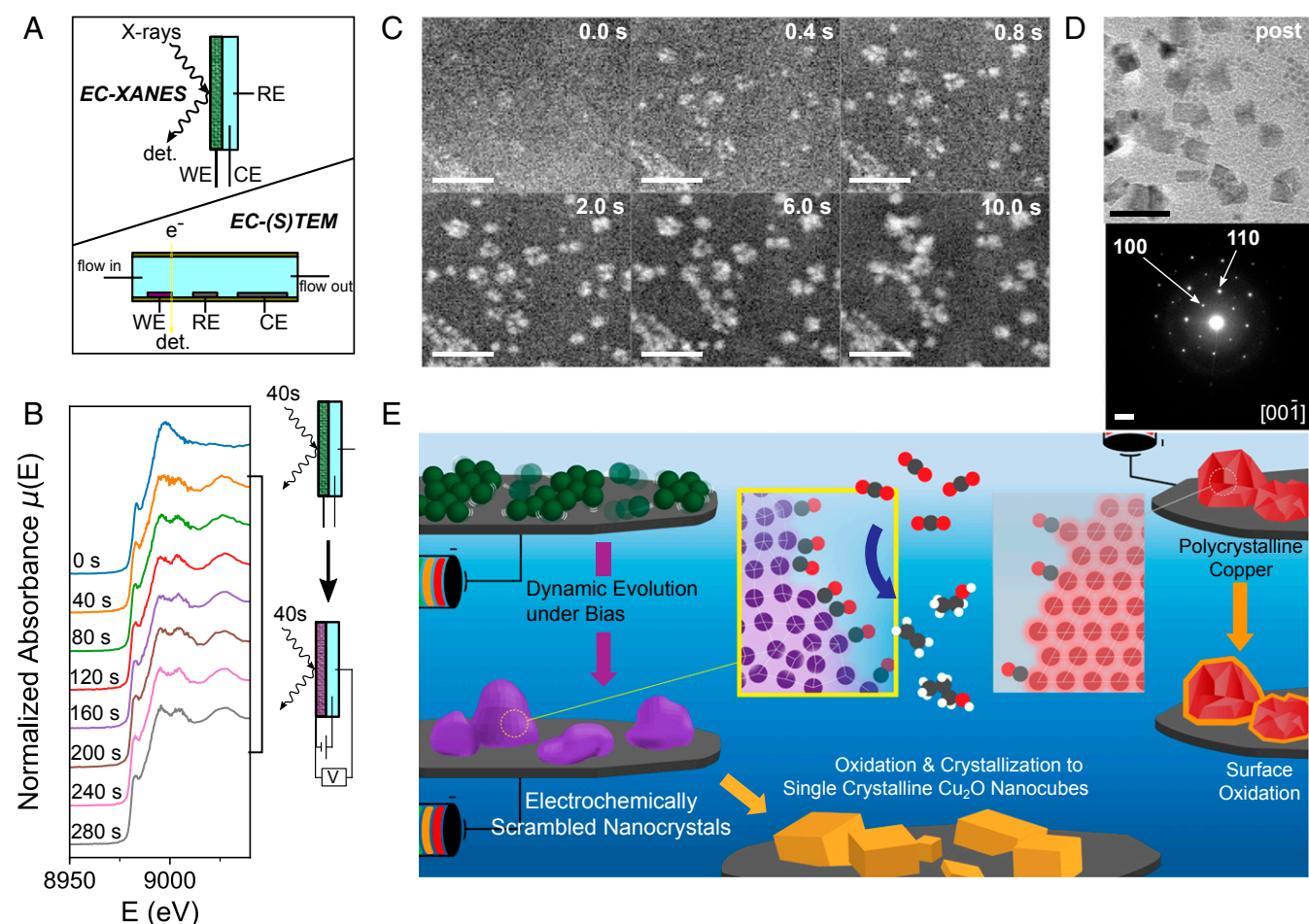
Fig. 4. In situ characterization of the Cu NP ensemble evolution under bias. (A) Configurations used for in situ EC-XANES and EC-(S)TEM. (B) EC-XANES with the initial (top) scan at open circuit and the remainder during bias at -0.6 V vs. RHE. (C) EC-HAADF-STEM of the 7-nm Cu NP system taken over a 10-s biasing period (frames from Movie S1; scale bars, 100 nm). (D) Ex situ TEM of the EC-STEM electrode after biasing, showing the expected NP-to-cube evolution (scale bar, 100 nm), with NBED showing single-crystal Cu_2O (Scale bar, 2 nm^{-1}). (E) Unified description of electrochemically scrambled nanocrystals with disordered surfaces that enhance CO_2-to-C_{2+}, vs. relatively inactive polycrystalline Cu nanocrystals.

Appendix, Fig. S13). These in situ results confirm that the evolution process unique to sample O occurs rapidly, on the order of seconds. Further resolution of the structural details of these systems was limited due to the NPs' dynamic nature (*SI Appendix, Supplementary Discussion S3* and Movies S3 and S4).

In conjunction with our ex situ observations, we find that electrochemical bias induces rapid fusion of an NP ensemble into a disordered metallic steady state (sample O) with high C_{2+} selectivity and intrinsic C–C activity, which we term scrambling (Fig. 4*E*). This relative loss of atomic order is likely what triggers a complete "recrystallization" to a single crystalline Cu_2O nanocube on air exposure. The effect is largest for small nanocrystals, owing to their higher energy increasing the tendency for free atomic migration upon bias as represented by their high mobility. In contrast, larger NPs scramble to a lesser extent, while redox pulses allow periods of oxide crystallization to interrupt the scrambling process, resulting in samples L/P exhibiting more typical polycrystalline Cu structures surrounded by oxide shells. The disorder-derived active surfaces arising from scrambling exhibits increased electrochemical binding strength, which potentially translates to a higher population of strongly bound *CO. This effect may be related to previous reports of disorder-induced microstrain modulating electrocatalytic activity (34). Additionally, relaxing the geometric constraint of crystallinity may allow configurations that alleviate the undesired repulsive interactions of a high density of bound *CO (35), comparable to the creation of optimal geometries in enzymatic systems. The sum of these effects potentially contributes to the overpotential reduction toward C–C coupling in the scrambled nanocrystal system. Catalysts exhibiting a lower degree of disorder (e.g., samples L/P) thus are only able to yield comparable C_{2+} activity at elevated potentials (−0.9 V and beyond) (*SI Appendix*, Fig. S45).

The mechanism of disorder development in the scrambled NP system should stem from the structural details of the original NP. For instance, the fivefold twinned 7-nm NP structure contains a high proportion of atoms at grain boundaries, where disorder-forming processes such as premelting are observed in model crystal systems (36). The disorder may also be intrinsic to the effect of reducing an oxide shell, as is present on the original NPs and has been suggested previously (18). However, since not every reduced oxide can achieve the same catalytic activity (as shown by the Cu_2O cubes as-grown), the NP fusion involved in the scrambled system is likely to be critical to preserving such characteristics. For example, as the fusion occurs within the NP ensemble, the presence of a high grain boundary density may result in pinned crystallite junctions that impede boundary migration and crystal growth as evolution proceeds (37). Additional factors not presently investigated, such as the behavior of surface ligands under bias, may also play a role. Eventually, unraveling the atomistic details of the electrochemical nanocrystal scrambling process will contend with the complex interplay among an ensemble of particles composed of nanoscale-twinned Cu cores, thin Cu_2O shells, and surrounding ligands, under biased conditions. Additionally, the question of how it is maintained raises an intriguing opportunity to understand the structural requirements for its sustenance, in the context of translating such insights to other materials. We expect more advanced *operando* techniques as well as cryo–X-ray absorption spectroscopy (XAS) (38) to yield important new insights, presenting opportunities for designing catalysts with the necessary characteristics to attain similarly active states.

In conclusion, we have comprehensively probed the dynamic fusion of Cu NPs under CO_2 reducing conditions to form multicarbon-active scrambled nanocrystals. These structures are described by three distinct signatures: ex situ formation of single-crystal oxide cubes, low coordination and crystallinity after passivation, and high mobility observed in situ. Together, these

observations suggest an enriched disorder in the copper phase with substantially enhanced intrinsic CO_2-to-C_{2+} compared to crystalline Cu, motivating closer investigation into the atomic details of low-crystallinity Cu surface motifs and their preservation throughout. Moreover, we emphasize that a full understanding of active catalysts, which are more likely to be structurally unstable, will require ex situ, quasi-in situ, and *operando* techniques explored in concert.

Materials and Methods

NP Synthesis and Electrode Fabrication. Seven-nanometer copper NPs were synthesized as previously reported (23). For larger NPs, size was controlled by tuning the mole ratio of tetradecylphosphonic acid to copper(I) acetate (CuAc), where higher ratio resulted in larger particles. Specifically, to synthesize 7-, 9-, 14-, and 20-nm NPs, ratios of 0.5, 0.7, 1, and 1.25, respectively, were used while maintaining the absolute concentration of CuAc (1 mmol).

NP concentrations by mass of copper were measured by inductively coupled plasma optical emission spectroscopy, after which 68.9 μg of copper was deposited on 1-cm^2 area of carbon paper (Sigracet 29AA; Fuel Cell Store) to make working electrodes. Larger NPs were deposited in a similar manner with identical mass loading.

For electrochemically grown Cu_2O nanocubes, a square-wave voltammetric pulse program was employed as reported previously. Cu_2O nanocubes were directly grown on carbon paper (Sigracet 29AA) (39).

For copper foil-derived electrodes, copper foil (99.9999%; Alfa Aesar) was electropolished in 85% H_3PO_4 at 3 V for 3 min against a copper counterelectrode. Electrochemically cycled oxide-derived copper was then fabricated following the method previously reported for EC–Cu (14).

Electrochemical Evolution of NPs and Catalytic Activity Measurements. The customized electrochemical setup used to carry out bias-induced evolution of NPs and catalytic testing has been described previously (23). All electrochemical measurements were made against a 3 M KCl Ag/AgCl reference electrode (World Precision Instruments). For all biasing experiments, the bias was applied directly without a prior linear sweep. Evolution was typically carried out by directly applying −1.2 V vs. Ag/AgCl, while catalytic results were measured at −1.45 V vs. Ag/AgCl. These potentials were considered equivalent by the steady-state structure made, as elaborated upon in *SI Appendix*, Fig. S3. All chronoamperometry was corrected with 85% of the solution resistance (Biologic), with the remaining 15% corrected afterward. Gas and liquid products were measured by a gas chromatograph [equipped with a thermal conductivity detector and a flame ionization detector with methanizer (SRI)] and NMR with water suppression (Bruker Avance 500), respectively.

For pulsed preparation of sample P, the potential was varied between −1.2 V vs. Ag/AgCl and 0.0 V vs. Ag/AgCl with periods of 2.5 s each. This pulse program was repeated 240 times, for a total of 1200 s of bias, before the potential was immediately switched to −1.45 V vs. Ag/AgCl for catalytic testing.

Passivation with BTA (Sigma-Aldrich 99%) was conducted after electrolysis by removing the electrode from the cell and, within a short period time, immersing the electrode in a premade 10 mL bath of BTA dissolved in CO_2-saturated 0.1 M $KHCO_3$. The amount of BTA was set to a mole ratio of 1000 mol BTA to 1 mol Cu (the maximum concentration shown in *SI Appendix*, Fig. S22).

Lead underpotential deposition was conducted immediately post-electrolysis in a solution of 0.1 M $NaClO_4$, 10 mM $HClO_4$, and 3 mM $Pb(II)(ClO_4)_2$. Cyclic voltammetry in the Pb underpotential region was conducted at 10 mV/s six times, for which the cycles were confirmed consistent and the fifth scan was reported. The potentials are referenced against a 1.0 M KCl Ag/AgCl electrode.

Ex Situ Structural Characterization. Electrodes were directly imaged by SEM (Ultra 55-FESEM), and samples were crushed into a fine powder for powder X-ray diffraction (Bruker D8). For TEM sample preparation, the carbon paper electrode was crushed into a fine powder and dropcast on a TEM grid, typically lacey carbon, from a dispersion in toluene. Low magnification TEM (Hitachi H-7650) was conducted at 100 kV, while HRTEM and STEM-EELS (Tecnai F20 UT) were conducted at 200 kV. NBED, along with additional HRTEM (JEOL 2100-F), were also conducted at 200 kV. XPS (K-Alpha ; Thermo Scientific) was measured using an Al Ka source with spectra collected at a pass energy of 20 eV and step size of 0.05 eV.

XAS. XAS experiments were conducted at the Advanced Light Source X-Ray Fluorescence Microprobe beamline 10.3.2 following previously reported procedures for Cu NPs (40). All data were recorded in fluorescence using quick-XAS (QXAS) mode [where the Si(111) is scanned on the fly], using a seven-element Ge solid-state fluorescence detector. Energy calibration was performed using a Cu foil (first derivative maximum set at 8980.48 eV) (41). For ex situ measurements, electrodes were biased in the typical manner and removed for measurement under ambient conditions. Cu K-edge XANES data processing (deadtime correction, deglitching, energy calibration, preedge background substraction, and postedge normalization), and least-square linear combination fits (LCF), were conducted with the LabVIEW custom software available at https://sites.google.com/lbl.gov/lbnl-als-1032/software-download. In addition, LCFs were performed in Athena for corroboration; the variation of phase contributions between these two programs did not exceed 5% in all cases.

EXAFS data reduction was performed in Athena and EXAFS fitting was performed in Artemis according to previous procedures (40). Both programs are part of Demeter package 0.9.26 (42). For EXAFS data fitting of the various Cu samples, two FEFF models of Cu metal and Cu_2O were generated. They were made according to the well-known crystal structure (both face-centered cubic with respect to Cu) of the bulk materials. All Cu NPs samples were fit using the first three single scattering paths and the collinear triple scattering path to the fourth shell from Cu metal, as well as the first O single scattering path in Cu_2O. Addition of the first Cu single scattering path in Cu_2O was required to fit the samples containing a more prominent oxide phase.

In situ XAS was conducted in a custom-designed polyether ether ketone electrochemical cell. A working electrode was fabricated by depositing Cu NPs over a 1-cm^2 area of carbon paper (Sigracet 29AA), which was pressed against a 300-μm Kapton window. The cell was filled and constantly purged at under 1 sccm with 0.1 M $KHCO_3$ kept under CO_2 saturation. Open circuit voltage was measured during purging, and XANES scans were taken after the cell was completely filled. To begin electrochemical evolution, −1.3 V vs. Ag/AgCl was applied vs. the 3 M KCl Ag/AgCl reference electrode with a glassy carbon counter electrode. Due to the rapid structure evolution under bias, the XANES spectral range was shortened so that each spectrum took only ∼40 s, increasing temporal resolution for qualitative study. Depending on the desired duration of bias, 1 to 20 QXAS lines were measured before electrolysis was stopped and the cell disassembled under ambient conditions.

In Situ Electron Microscopy. All in situ electron microscopy was conducted at 200 kV (2100-F; JEOL). Commercial electrochemical TEM chips (XL P7 carbon electrochemical chip; Hummingbird) were used with a 500-nm silicon nitride spacer (Hummingbird), such that the total assembly included 100 nm of silicon nitride and 500 nm of liquid volume. All biasing leads were carbon-coated Pt as supplied by the manufacturer.

To create working electrodes, a 2-μL droplet of a dilute (25 μg/mL) solution of Cu NPs in hexanes was spread over the viewing area of the chip. The droplet was allowed to evaporate, after which the full cell was assembled. Three hundred microliters of ethanol were first purged through, after which 1 to 1.5 mL of 0.1 M $KHCO_3$ or pure H_2O were purged at 10 μL/min in order to wet and fill up the entire cell. Control experiments were conducted with Pt/C particles (20 wt % nominal; Alfa Aesar) using a similar loading strategy, without ethanol purging.

Electrochemical testing was conducted in a specially designed biasing holder (Hummingbird) with a floating potentiostat (Gamry Interface 1000), using a three-electrode configuration. The biasing potential was set at −0.6 V vs. the carbon pseudoreference electrode, at which chronoamperometry using a typical cell produced ∼500 nA of reductive current. Higher currents/potentials (e.g., >1 μA at −0.8 V vs. the carbon pseudoreference) were deemed unsuitable due to violent ruptures of the electrochemical cell, while significantly lower currents (i.e., order of 10 to 100 nA) failed to reproduce the cubic oxide structures postelectrolysis in favor of adventitious side reactions such as the growth of polycrystalline copper.

During bias, electrolyte purging was halted. Real-time videos were recorded using a screen capture program at five frames per second, matching both the raster rate of the STEM beam over the viewing frame and the exposure time of the camera during bright-field TEM. After electrochemical imaging experiments, the holder was disconnected from the potentiostat. The cell was then directly disassembled and the working chip rinsed gently with H_2O before drying under N_2. The chip was then imaged by TEM and NBED (JEOL 2100-F) under vacuum conditions.

1. F. F. Tao, P. A. Crozier, Atomic-scale observations of catalyst structures under reaction conditions and during catalysis. *Chem. Rev.* **116**, 3487–3539 (2016).
2. F. Tao *et al.*, Reaction-driven restructuring of Rh-Pd and Pt-Pd core-shell nanoparticles. *Science* **322**, 932–934 (2008).
3. C. Cui, L. Gan, M. Heggen, S. Rudi, P. Strasser, Compositional segregation in shaped Pt alloy nanoparticles and their structural behaviour during electrocatalysis. *Nat. Mater.* **12**, 765–771 (2013).
4. V. Beermann *et al.*, Real-time imaging of activation and degradation of carbon supported octahedral Pt-Ni alloy fuel cell catalysts at the nanoscale using *in situ* electrochemical liquid cell STEM. *Energy Environ. Sci.* **12**, 2476–2485 (2019).
5. J. Huang *et al.*, Potential-induced nanoclustering of metallic catalysts during electrochemical CO_2 reduction. *Nat. Commun.* **9**, 3117 (2018).
6. Y.-G. G. Kim, J. H. Baricuatro, A. Javier, J. M. Gregoire, M. P. Soriaga, The evolution of the polycrystalline copper surface, first to Cu, (111) and then to Cu(100), at a fixed CO2RR potential: A study by operando EC-STM. *Langmuir* **30**, 15053–15056 (2014).
7. C. M. Gunathunge *et al.*, Spectroscopic observation of reversible surface reconstruction of copper electrodes under CO_2 reduction. *J. Phys. Chem. C* **121**, 12337–12344 (2017).
8. Z. Weng *et al.*, Active sites of copper-complex catalytic materials for electrochemical carbon dioxide reduction. *Nat. Commun.* **9**, 415 (2018).
9. S. Nitopi *et al.*, Progress and perspectives of electrochemical CO_2 reduction on copper in aqueous electrolyte. *Chem. Rev.* **119**, 7610–7672 (2019).
10. H. Mistry *et al.*, Highly selective plasma-activated copper catalysts for carbon dioxide reduction to ethylene. *Nat. Commun.* **7**, 12123 (2016).
11. C. W. Li, J. Ciston, M. W. Kanan, Electroreduction of carbon monoxide to liquid fuel on oxide-derived nanocrystalline copper. *Nature* **508**, 504–507 (2014).
12. K. Jiang *et al.*, Metal ion cycling of Cu foil for selective C–C coupling in electrochemical CO2 reduction. *Nat. Catal.* **1**, 111–119 (2018).
13. T. T. H. Hoang, S. Ma, J. I. Gold, P. J. A. Kenis, A. A. Gewirth, Nanoporous copper films by additive-controlled electrodeposition: CO_2 reduction catalysis. *ACS Catal.* **7**, 3313–3321 (2017).
14. Y. Lum, B. Yue, P. Lobaccaro, A. T. Bell, J. W. Ager, Optimizing C–C coupling on oxide-derived copper catalysts for electrochemical CO_2 reduction. *J. Phys. Chem. C* **121**, 14191–14203 (2017).
15. A. D. Handoko *et al.*, Mechanistic insights into the selective electroreduction of carbon dioxide to ethylene on Cu2O-derived copper catalysts. *J. Phys. Chem. C* **120**, 20058–20067 (2016).
16. Y. Kwon, Y. Lum, E. L. Clark, J. W. Ager, A. T. Bell, CO2 electroreduction with enhanced ethylene and ethanol selectivity by nanostructuring polycrystalline copper. *ChemElectroChem* **3**, 1012–1019 (2016).
17. H. Wang *et al.*, Rapid and scalable synthesis of cuprous halide-derived copper nanoarchitectures for selective electrochemical reduction of carbon dioxide. *Nano Lett.* **19**, 3925–3932 (2019).
18. A. Eilert *et al.*, Subsurface oxygen in oxide-derived copper electrocatalysts for carbon dioxide reduction. *J. Phys. Chem. Lett.* **8**, 285–290 (2017).
19. C. Hahn *et al.*, Engineering Cu surfaces for the electrocatalytic conversion of CO_2: Controlling selectivity toward oxygenates and hydrocarbons. *Proc. Natl. Acad. Sci. U.S.A.* **114**, 5918–5923 (2017).
20. D. Ren, J. Fong, B. S. Yeo, The effects of currents and potentials on the selectivities of copper toward carbon dioxide electroreduction. *Nat. Commun.* **9**, 925 (2018).
21. X. Feng, K. Jiang, S. Fan, M. W. Kanan, A direct grain-boundary-activity correlation for CO electroreduction on Cu nanoparticles. *ACS Cent. Sci.* **2**, 169–174 (2016).
22. H. Li, Y. Li, M. T. M. Koper, F. Calle-Vallejo, Bond-making and breaking between carbon, nitrogen, and oxygen in electrocatalysis. *J. Am. Chem. Soc.* **136**, 15694–15701 (2014).
23. D. Kim, C. S. Kley, Y. Li, P. Yang, Copper nanoparticle ensembles for selective electroreduction of CO_2 to C$_2$-C$_3$ products. *Proc. Natl. Acad. Sci. U.S.A.* **114**, 10560–10565 (2017).

24. K. Manthiram, B. J. Beberwyck, A. P. Alivisatos, Enhanced electrochemical methanation of carbon dioxide with a dispersible nanoscale copper catalyst. *J. Am. Chem. Soc.* **136**, 13319–13325 (2014).

25. E. D. Goodman, J. A. Schwalbe, M. Cargnello, Mechanistic understanding and the rational design of sinter-resistant heterogeneous catalysts. *ACS Catal.* **7**, 7156–7173 (2017).

26. J. M. Tranquada, S. M. Heald, A. R. Moodenbaugh, X-ray-absorption near-edge-structure study of La$_{2-x}$(Ba,Sr)$_x$CuO$_{4-y}$ superconductors. *Phys. Rev. B Condens. Matter* **36**, 5263–5274 (1987).

27. B. Beverskog, I. Puigdomenech, Revised pourbaix diagrams for copper at 25 to 300°C. *J. Electrochem. Soc.* **144**, 3476 (1997).

28. Y. Lum, J. W. Ager, Stability of residual oxides in oxide-derived copper catalysts for electrochemical CO$_2$ reduction investigated with ^{18}O labeling. *Angew. Chem. Int. Ed. Engl.* **57**, 551–554 (2018).

29. M. Finšgar, I. Milošev, Inhibition of copper corrosion by 1,2,3-benzotriazole: A review. *Corros. Sci.* **52**, 2737–2749 (2010).

30. B. K. Teo, H. S. Chen, R. Wang, M. R. Antonio, EXAFS of glassy metallic alloys: Amorphous and crystalline MoNi. *J. Non-Cryst. Solids* **58**, 249–274 (1983).

31. F. Cavalca *et al.*, Nature and distribution of stable subsurface oxygen in copper electrodes during electrochemical CO2 reduction. *J. Phys. Chem. C* **121**, 25003–25009 (2017).

32. G. M. Brisard, E. Zenati, H. A. Gasteiger, N. M. Marković, P. N. Ross, Underpotential deposition of lead on Cu(100) in the presence of chloride: Ex-situ low-energy electron diffraction, auger electron spectroscopy, and electrochemical studies. *Langmuir* **13**, 2390–2397 (1997).

33. C. Kim, T. Möller, J. Schmidt, A. Thomas, P. Strasser, Suppression of competing reaction channels by Pb adatom decoration of catalytically active Cu surfaces during CO2 electroreduction. *ACS Catal.* **9**, 1482–1488 (2019).

34. S. Kühl *et al.*, Concave curvature facets benefit oxygen electroreduction catalysis on octahedral shaped PtNi nanocatalysts. *J. Mater. Chem. A Mater. Energy Sustain.* **7**, 1149–1159 (2019).

35. B. Eren *et al.*, Activation of Cu(111) surface by decomposition into nanoclusters driven by CO adsorption. *Science* **351**, 475–478 (2016).

36. A. M. Alsayed, M. F. Islam, J. Zhang, P. J. Collings, A. G. Yodh, Premelting at defects within bulk colloidal crystals. *Science* **309**, 1207–1210 (2005).

37. E. A. Holm, S. M. Foiles, How grain growth stops: A mechanism for grain-growth stagnation in pure materials. *Science* **328**, 1138–1141 (2010).

38. A. Bergmann *et al.*, Reversible amorphization and the catalytically active state of crystalline Co3O4 during oxygen evolution. *Nat. Commun.* **6**, 8625 (2015).

39. X. Guo, W. Lv, X.-Y. Li, Additive-free shape-invariant nano-to-micron size-tuning of Cu$_2$O cubic crystals by square-wave voltammetry. *J. Phys. Chem. C* **118**, 11062–11077 (2014).

40. D. Kim, N. Becknell, Y. Yu, P. Yang, Room-temperature dynamics of vanishing copper nanoparticles supported on silica. *Nano Lett.* **17**, 2732–2737 (2017).

41. S. Kraft, J. Stümpel, P. Becker, U. Kuetgens, High resolution x-ray absorption spectroscopy with absolute energy calibration for the determination of absorption edge energies. *Rev. Sci. Instrum.* **67**, 681–687 (1996).

42. B. Ravel, M. Newville, ATHENA, ARTEMIS, HEPHAESTUS: Data analysis for X-ray absorption spectroscopy using IFEFFIT. *J. Synchrotron Radiat.* **12**, 537–541 (2005).